

Eclipse Mapping: Astrotomography of Accretion Discs

Raymundo Baptista

Abstract The Eclipse Mapping Method is an indirect imaging technique that transforms the shape of the eclipse light curve into a map of the surface brightness distribution of the occulted regions. Three decades of application of this technique to the investigation of the structure, the spectrum and the time evolution of accretion discs around white dwarfs in cataclysmic variables have enriched our understanding of these accretion devices with a wealth of details such as (but not limited to) moving heating/cooling waves during outbursts in dwarf novae, tidally-induced spiral shocks of emitting gas with sub-Keplerian velocities, elliptical precessing discs associated to superhumps, and measurements of the radial run of the disc viscosity through the mapping of the disc flickering sources. This chapter reviews the principles of the method, discusses its performance, limitations, useful error propagation procedures, and highlights a selection of applications aimed at showing the possible scientific problems that have been and may be addresses with it.

1 Context and Motivations

In weakly-magnetic cataclysmic variables (CVs) a late-type star overfills its Roche lobe and feeds a companion white dwarf (WD) via an accretion disc, which usually dominates the ultraviolet and optical light of the system [60]. The temperatures in CV discs may vary from 5000 K in the outer regions to over 50000 K close to the disc centre, and the surface density may vary by equally significant amounts over the disc surface. Therefore, the spectrum emitted by different regions of the accretion disc may be very distinct. Furthermore, aside of the component stars and the accretion disc, additional sources contribute to the integrated light from the binary: a bright spot (BS) or stream forms where the gas from the mass-donor star hits the

Raymundo Baptista
Departamento de Física, UFSC, Campus Trindade, 88040-900, Florianópolis, Brazil, e-mail: raybap@gmail.com

outer edge of the disc, tidally-induced spiral structures might develop in the outer regions of extended discs [59, 8], and a fraction of the transferred mass may also be ejected from the binary in a wind from the disc surface [9, 38]. Because what one directly observes is the combination of the spectra emitted from these diverse regions and sources, the interpretation of CVs observations is usually plagued by the ambiguity associated with composite spectra. The most effective way to overcome these difficulties is with spatially resolved data, in which the light from the different sources might be disentangled. However, at typical sizes of less than a solar radius and distances of hundreds of parsecs, accretion discs in CVs are seen at angular diameters of tens of micro-arcseconds, and spatially resolving them is well beyond the reach of current direct imaging interferometric techniques, both at optical and radio wavelength ranges. Thus, resolving an accretion disc in a CV is presently possible only via indirect imaging.

Developed in the 1980's by Horne [33], the Eclipse Mapping Method is an indirect imaging technique which provides spatially resolved observational constraints of accretion discs in CVs on angular scales of micro-arcseconds. It assembles the information contained in the shape of the eclipse into a map of the accretion disc surface brightness distribution. The following sections describe the technique and provide a set of examples aiming at illustrating the wealth of possible applications.

2 Principles & Inner Workings

The three basic assumptions of the standard eclipse mapping method are: (i) the surface of the secondary star is given by its Roche equipotential, (ii) the brightness distribution is constrained to the orbital plane, and (iii) the emitted radiation is independent of the orbital phase. While assumption (i) is reasonably robust and always employed, the others are simplifications that do not hold in all situations and may be relaxed with three-dimensional (3D) eclipse mapping implementations (see Sect. 5.4).

A grid of intensities centred on the WD, the eclipse map, is defined in the orbital plane. One usually adopts the distance from the disc centre to the internal Lagrangian point, R_{L1} , as the length scale. With this definition the primary lobe has about the same size and form for any reasonable value of the binary mass ratio q ($=M_2/M_1$, where M_2 and M_1 are the masses of the mass-donor star and the WD, respectively) [33]. If the eclipse map is an N points flat, square grid of side λR_{L1} , each of its surface element (pixel) has an area $(\lambda R_{L1})^2/N$ and an associated intensity I_j . The solid angle comprised by each pixel as seen from the earth is then

$$\theta^2 = \left[\frac{(\lambda R_{L1})^2}{N} \frac{1}{d^2} \right] \cos i, \quad (1)$$

where d is the distance to the system. The value of λ defines the area of the eclipse map while the choice of N sets its spatial resolution.

The model eclipse light curve $m(\phi)$ is derived from the intensities in the eclipse map,

$$m(\phi) = \theta^2 \sum_{j=1}^N I_j V_j(\phi) . \quad (2)$$

The eclipse geometry $V_j(\phi)$ specifies the fractional visibility of each pixel as a function of orbital phase and may include fore-shortening and limb darkening factors [35, 50, 65]. The fractional visibility of a given pixel is obtained by dividing the pixel into smaller tiles and evaluating the Roche potential along the line of sight for each tile to see if the potential falls below the value of the equipotential that defines the Roche surface of the mass-donor star. If so, the tile is occulted. The fractional visibility of the pixel is then the sum of the visible tiles divided by the number of tiles.

The eclipse geometry is determined by the inclination i , the binary mass ratio q and the phase of inferior conjunction ϕ_0 [33, 35]. These parameters set the shape and extension of the projected shadow of the mass-donor star in the orbital plane. As the binary phase ϕ changes during eclipse, the resulting shadow rotates around the L1 point, progressively covering/uncovering different parts of the accretion disc. This creates a grid of criss-crossed ingress/egress arcs in the orbital plane. A pixel with coordinates (x, y) within the region covered by this grid disappears and reappears from eclipse at a particular pair of binary phases (ϕ_i, ϕ_e) ¹. Thus, the eclipse geometry sets the connection between the image space (the eclipse map) and the data space (the light curve).

Figure 1 shows an example of eclipse geometry and depicts the connection between the image and data spaces. Information about the location of the occulted brightness sources is embedded in the shape of the eclipse light curve. The width of the eclipse increases as the light source moves closer to the L1 point, whereas it is displaced towards negative (positive) phases if the light source is in the leading (trailing) disc side. For example, the phase width and range of the eclipse in the upper right panel of Fig. 1 tells us that the corresponding light source (the blue pixel in the left-hand panel of Fig. 1) is located in the leading, near side of the disc. Figure 2 illustrates the simulation of the eclipse of a fitted brightness distribution while showing the comparison between the resulting model light curve and the data light curve. The geometry in this case is $i = 81^\circ$ and $q = 0.5$. The left-hand panels show the data light curve (small dots) and the model light curve (solid line) as it is being drawn at five different orbital phases along the eclipse (indicated in the upper right corner). The right-hand panels show the best-fit disc brightness distribution and how it is progressively covered by the dark shadow of the mass-donor star during the eclipse. The slope of the light curve steepens whenever a bright source is occulted or reappears from eclipse. The two asymmetric arcs of the brightness distribution of this example are occulted at distinct phases, leading to a V-shaped

¹ Pixels outside the region covered by the grid of criss-crossed arcs are never eclipsed, and have no corresponding ingress/egress phases (ϕ_i, ϕ_e) . Accordingly, there is no information about the surface brightness distribution of these unocculted regions in the shape of the eclipse.

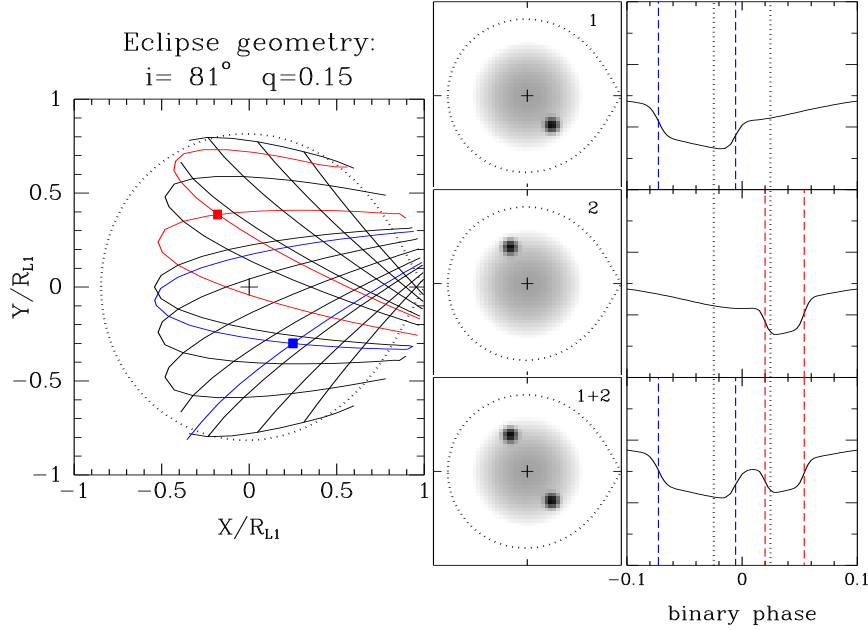


Fig. 1 Left-hand panel: A grid of criss-crossed ingress/egress arcs for the eclipse geometry $i = 81^\circ$, $q = 0.15$, and an eclipse map with $\lambda = 2$. The ingress/egress arcs for the blue and red pixels are shown in the respective colour. A dotted line depicts the primary Roche lobe; a cross marks the disc centre. The mass-donor star is to the right of the panel and the stars rotate counter-clockwise (equivalently, the observer and the mass-donor star shadow rotate clockwise). Middle-panels: grayscale brightness distributions with a faint, extended disc plus bright, narrow Gaussian spots at the positions of the blue and red pixels in the left panel. Right-hand panels: the model eclipse light curves obtained by convolving the eclipse geometry in the left panel with the brightness distributions in the middle panels. Vertical dotted lines mark the ingress/egress of the disc centre; blue/red vertical dashed lines depict the ingress/egress phases of the blue/red pixels.

eclipse with two bulges at ingress and at egress. The flux at phase $\phi = 0$ does not go to zero because a sizeable fraction of the disc remains visible at mid-eclipse.

Given the eclipse geometry, a model light curve can be calculated for any assumed brightness distribution in the eclipse map. A computer code then iteratively adjusts the intensities in the map (treated as independent parameters) to find the brightness distribution the model light curve of which fits the data eclipse light curve within the uncertainties (Fig. 3). Because the one-dimensional data light curve cannot fully constrain a two-dimensional map, additional freedom remains to optimise some map property. A maximum entropy (MEM) procedure [56, 57] is used to select, among all possible solutions, the one that maximises the entropy of the eclipse map with respect to a smooth default map.

The entropy of the eclipse map p with respect to the default map q is defined as

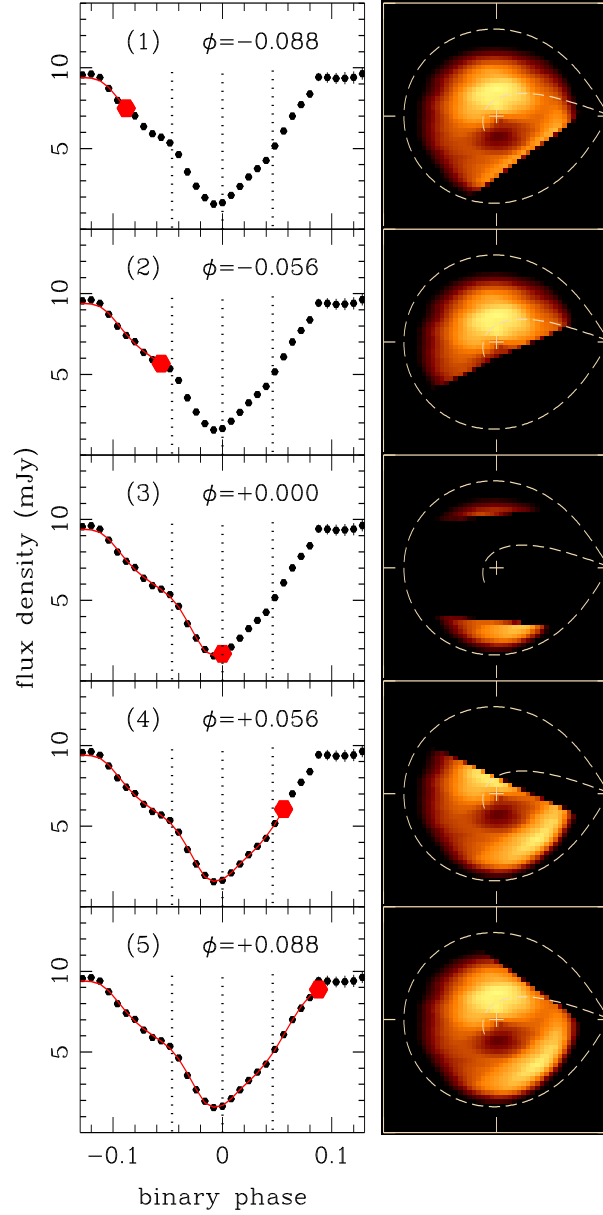


Fig. 2 Simulation of a disc eclipse ($i = 81^\circ$, $q = 0.5$). Left-hand panels: data light curve (dots) and model light curve (solid line) at five different binary phases (indicated in the upper right corner). Vertical dotted lines mark mid-eclipse and the ingress/egress phases of the disc centre. Right-hand panels: visible parts of the best-fit eclipse map (in a false colour blackbody logarithmic scale) at the corresponding binary phases. Dashed lines show the primary Roche lobe and the ballistic trajectory of the gas from the mass-donor star; crosses mark the centre of the disc. The mass-donor star is to the right of each panel; the stars and the accretion disc gas rotate counter-clockwise.

$$S = - \sum_{j=1}^N p_j \ln \left(\frac{p_j}{q_j} \right), \quad (3)$$

where p and q are written as

$$p_j = \frac{I_j}{\sum_k I_k}, \quad q_j = \frac{D_j}{\sum_k D_k}. \quad (4)$$

Other functional forms for the entropy appear in the literature [35, 60]. These are equivalent to (3) when p and q are written in terms of proportions.

The default map D_j is generally defined as a weighted average of the intensities in the eclipse map,

$$D_j = \frac{\sum_k \omega_{jk} I_k}{\sum_k \omega_{jk}}, \quad (5)$$

where the weight function ω_{jk} is specified by the user. A priori information about the disc (e.g., axi-symmetry) is included in the default map via ω_{jk} . Prescriptions for the weight function ω_{jk} and their effect in the reconstructions are discussed in Sect. 3. In the absence of any constraints on I_j , the entropy has a maximum $S_{max} = 0$ when $p_j = q_j$, or when the eclipse map and the default map are identical.

The consistency of an eclipse map may be checked using the χ^2 as a constraint function,

$$\chi^2 = \frac{1}{M} \sum_{\phi=1}^M \left(\frac{m(\phi) - d(\phi)}{\sigma(\phi)} \right)^2 = \frac{1}{M} \sum_{\phi=1}^M r(\phi)^2, \quad (6)$$

where $d(\phi)$ is the data light curve, $\sigma(\phi)$ are the corresponding uncertainties, $r(\phi)$ is the residual at the orbital phase ϕ , and M is the number of data points in the light curve. Alternatively, the constraint function may be a combination of the χ^2 and the R-statistics [15],

$$R = \frac{1}{\sqrt{M-1}} \sum_{\phi=1}^{M-1} r(\phi) r(\phi+1), \quad (7)$$

to minimise the presence of correlated residuals in the model light curve [14]. For the case of uncorrelated normally distributed residuals, the R-statistics has a Gaussian probability distribution function with average zero and unity standard deviation. Requiring the code to achieve an $R = 0$, is equivalent to asking for a solution with uncorrelated residuals in the model light curve.

The final MEM solution is the eclipse map that is as close as possible to its default map as allowed by the constraint imposed by the light curve and its associated uncertainties [35, 50]. In mathematical terms, the problem is one of constrained maximisation, where the function to maximise is the entropy and the constraint is a consistency statistics that measures the quality of the fitted model to the data light curve. Different codes exist to solve this problem. Many of the eclipse mapping codes are based on the commercial optimisation package MEMSYS [56]. Alternative implementations using conjugate-gradients algorithms [14, 15], CLEAN-like algorithms [58] and genetic algorithms [20] are also used.

Rutten et al. [52] found that the entropy function can be a useful tool to signal and to isolate the fraction of the total light which is not coming from the accretion disc plane. They noted that when the light curve is contaminated by the presence of additional light (e.g., from the mass-donor star) the reconstructed map shows a spurious structure in its outermost region. This is because the eclipse mapping method assumes that all the light is coming from the accretion disc, in which case the eclipse depth and width are correlated in the sense that a steeper shape corresponds to a deeper eclipse. The addition of an uneclipsed component in the light curve (i.e., light from a source other than the accretion disc) ruins this correlation. To account for the extra amount of light at mid-eclipse and to preserve the brightness distribution derived from the eclipse shape the algorithm inserts the additional light in the region of the map which is least affected by the eclipse. Since the entropy measures the amount of structure in the map, the presence of these spurious structures is flagged with lower entropy values. The correct offset level may be found by comparing a set of maps obtained with different offsets and selecting the one with highest entropy. Alternatively, the value of the zero-intensity level can be included in the mapping algorithm as an additional free parameter to be fitted along with the intensity map in the search for the MEM solution [9, 49]. A detailed discussion on the reliability and consistency of the estimation of the uneclipsed component can be found in [16].

Figure 3 gives an example of the convergence process of a MEM reconstruction. The code starts from a flat map and quickly evolves towards an axi-symmetric Gaussian map which reproduces the gross features of the data light curve. However, at this point the model light curve is not a good match to the data ($\chi^2 = 16.7$), failing to reproduce the double stepped ingress/egress bulges of the eclipse shape. Several more iterations are required in order to match these features in the data light curve, which demands building two asymmetric bright arcs in the leading and trailing sides of the disc. The reconstruction converges for a final unity χ^2 value after 233 iterations.

3 Performance & Limitations

A crucial aspects of eclipse mapping is the selection of the weight function for the default map, ω_{jk} , which allows the investigator to steer the MEM solution towards a determined type of disc map. The choice $\omega_{jk} = 1$ results in a uniform default map which leads to the *most uniform eclipse map* consistent with the data. This happens not to be a good choice for eclipse mapping, because it results in a map severely distorted by criss-crossed artefacts [19, 33, 58] as the flux of point sources is spread along their ingress and egress arcs (Fig. 4(a)). This led to the adoption of a weight function which sets the default map as an axi-symmetric average of the eclipse map, thereby yielding the *most nearly axi-symmetric map* that fits the data [33]. It suppresses the azimuthal information in the default map while keeping the radial structure of I_j on scales greater than a radial blur width Δ_R . This seems a

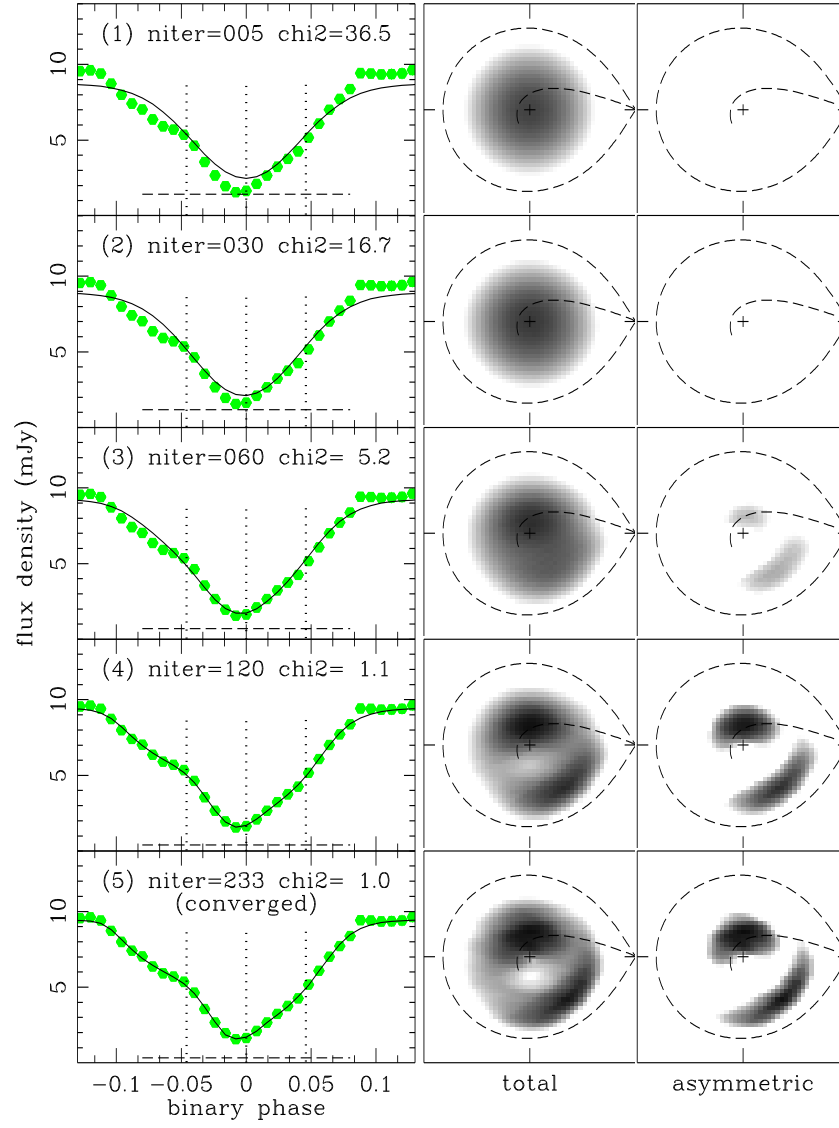


Fig. 3 Example of the iterative fit of a data light curve with a MEM eclipse mapping code [15]. Left-hand panels: data (points) and model (solid line) light curves at five different stages of the iteration process towards convergence. Vertical dotted lines mark mid-eclipse and the ingress/egress of the disc centre. A horizontal dashed line depicts the uneclipsed component of the total flux. *niter* and *chi2* give the current iteration number and χ^2 value, respectively. Middle panels: corresponding eclipse maps in a logarithmic grayscale; darker regions are brighter. The notation is the similar to that of Fig. 2. Right-hand panels: the asymmetric component of the eclipse maps in the middle panels.

reasonable choice for accretion disc mapping because one expects the disc material to be roughly in Keplerian orbits, so that local departures from axi-symmetry will tend to be smeared away by the strong shear. This is a commonly used option and is also known as the default map of full azimuthal smearing.

The full azimuthal smearing default results in rather distorted reproduction of asymmetric structures such as a bright spot at the disc rim. In this case, the reconstructed map exhibits a lower integrated flux in the asymmetric source region, the excess being redistributed as a concentric annulus about the same radial distance. By limiting the amount of azimuthal smearing it is possible to alleviate this effect and to start recovering azimuthal information in the accretion disc. Two prescriptions in this regard were proposed. Rutten et al. [47] limited the amount of azimuthal smearing by averaging over a polar Gaussian weight function of *constant angle* Δ_θ along the map²,

$$\omega_{jk} = \exp \left[-\frac{1}{2} \left(\frac{(R_j - R_k)^2}{\Delta_R^2} + \frac{\theta_{jk}^2}{\Delta_\theta^2} \right) \right] \quad (8)$$

while Baptista et al. [16] chose to use a polar Gaussian function of *constant arc length* Δ_s through the map,

$$\omega_{jk} = \exp \left[-\frac{1}{2} \left(\frac{(R_j - R_k)^2}{\Delta_R^2} + \frac{s_{jk}^2}{\Delta_s^2} \right) \right]. \quad (9)$$

The reconstructions in Figs. 4(b)-(d) used the default function of Eq. 8. In particular, the reconstructions in Figs. 4(a) and 4(b) were obtained from the same input light curve. This comparison illustrates that the default of limited azimuthal smearing provides a much better reconstruction of the central brightness distribution while still allowing to recover the location of a bright spot at disc rim, although with some azimuthal smearing.

The concept of default map was extended with the introduction of a double default function [19, 58, 11],

$$D_j = (D1_j)^n (D2_j)^m \quad (10)$$

(where $D1_j$ and $D2_j$ are separate default functions and $n + m = 1$), together with the idea of a negative default function (e.g., $m < 0$). While a positive default function steers the MEM solution *towards* its intrinsic property (e.g., axi-symmetry), a negative default function may be used to drive the MEM solution *away* from its intrinsic property (e.g., the presence of the undesired criss-crossed arcs) [58]. The combination of a positive axi-symmetric default function with a negative criss-crossed arcs default function was key to allow the recovery of accretion disc spiral structures with eclipse mapping [30, 11]. The eclipse maps shown in Figs. 2, 3 and 5 were obtained with this double default setup.

² R_j and R_k are the distances from pixels j and k to the centre of the disc; θ_{jk} is the azimuthal angle between pixels j and k ; s_{jk} is the arc-length between pixels j and k .

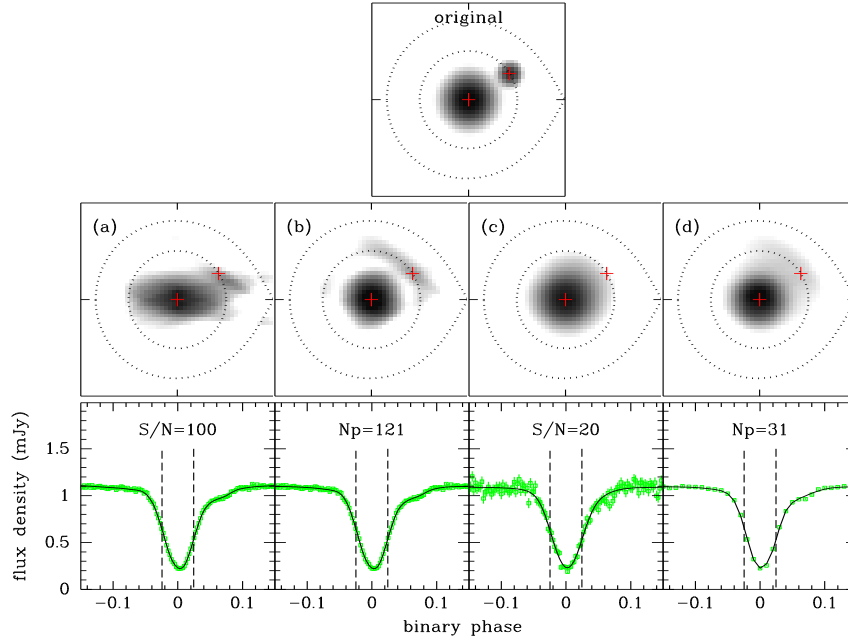


Fig. 4 Effects of the default map, phase resolution (= number of data points in the light curve) and signal-to-noise ratio (S/N) of the input data on the eclipse mapping reconstruction. The top panel shows an artificial, test brightness distribution in a logarithmic grayscale. The notation is similar to that of Fig. 1. The middle panels show reconstructions of the test brightness distribution for different combination of parameters: (a) uniform default map on a light curve with $N = 121$ data points and $S/N = 100$; (b) default of limited azimuthal smearing (Eq. 8), $Np = 121$ and $S/N = 100$; (c) default of Eq. 8, $Np = 121$ and $S/N = 20$; and (d) default of Eq. 8, $Np = 31$ and $S/N = 100$. The lower panels show the corresponding data (points) and model (solid line) light curves. Vertical dashed lines mark the ingress/egress phases of the disc centre.

The quality of an eclipse mapping reconstruction is tied to the quality of the input data light curve. Specifically, the ability to recover brightness sources and the spatial resolution of an eclipse map depend on the phase (or, time) resolution and the signal-to-noise ratio (S/N) of the data light curve. Baptista & Steiner [14] provide an expression to compute the spatial resolution of the eclipse map which matches the phase resolution of the data light curve. Fig. 4 shows the effects of (i) degrading the phase resolution and (ii) lowering the S/N of the data light curve on the quality of the resulting eclipse map. As a reference for comparison, the eclipse map in Fig. 4(b) was obtained from a light curve of good phase resolution ($Np = 121$ data points) and high signal-to-noise ($S/N = 100$). Fig. 4(c) shows that degrading the S/N reduces the ability to identify fainter brightness sources. Because of the reduced S/N , the model light curve is not forced to follow the egress shoulder that signals the presence of the bright spot at disc rim. As a consequence, the eclipse map has only a weak asymmetry at the position of the bright spot. Fig. 4(d) shows

that the effect of reducing the phase resolution in the light curve is to reduce the spatial resolution of the eclipse map, with an increase in the radial/azimuthal blur effects (i.e., point sources would look increasingly out of focus with decreasing phase resolution). The effects of low S/N seem more dramatic than those of low phase resolution.

4 Error Propagation Procedures

Because the maximum-entropy eclipse mapping is a non-linear inversion method, it is not possible to compute the uncertainties in the eclipse map directly from the uncertainties in the data light curve. Hence, statistical uncertainties of an eclipse map are usually computed with a Monte Carlo error propagation procedure [52]. This is illustrated in Fig. 5. A set of N (≥ 20) artificial light curves is created from the original data in which the flux at each phase is varied around the true value according to a Gaussian distribution with standard deviation equals to the uncertainty at that point. The artificial light curves are fitted with the eclipse mapping code to generate a set of randomised eclipse maps. These are then combined to produce a “residuals” map by taking the pixel-to-pixel standard deviation with respect to the mean intensity. This yields the statistical uncertainty at each pixel. For $N = 20$, the uncertainty of the standard deviation is $< 20\%$, sufficient to illustrate the confidence limits of the eclipse map, whereas $N \geq 200$ is needed in order to bring the uncertainty in the standard deviation down to 7% [30]. Uncertainties obtained with this procedure may be used to estimate the errors in the derived radial brightness temperature and intensity distributions. A map of the statistical significance (or the inverse of the relative error) is obtained by dividing the true eclipse map by the “residuals” map [30, 5, 11].

An alternative error propagation procedure involves the use of simulations with the Bootstrap technique (e.g., [6]).

5 Applications

This section focuses on selected applications of the eclipse mapping method which illustrates some of the possible scientific problems that have been and may be addresses with it. The reader is referred to [34, 35, 65, 2] for more comprehensive reviews of the results obtained with this technique.

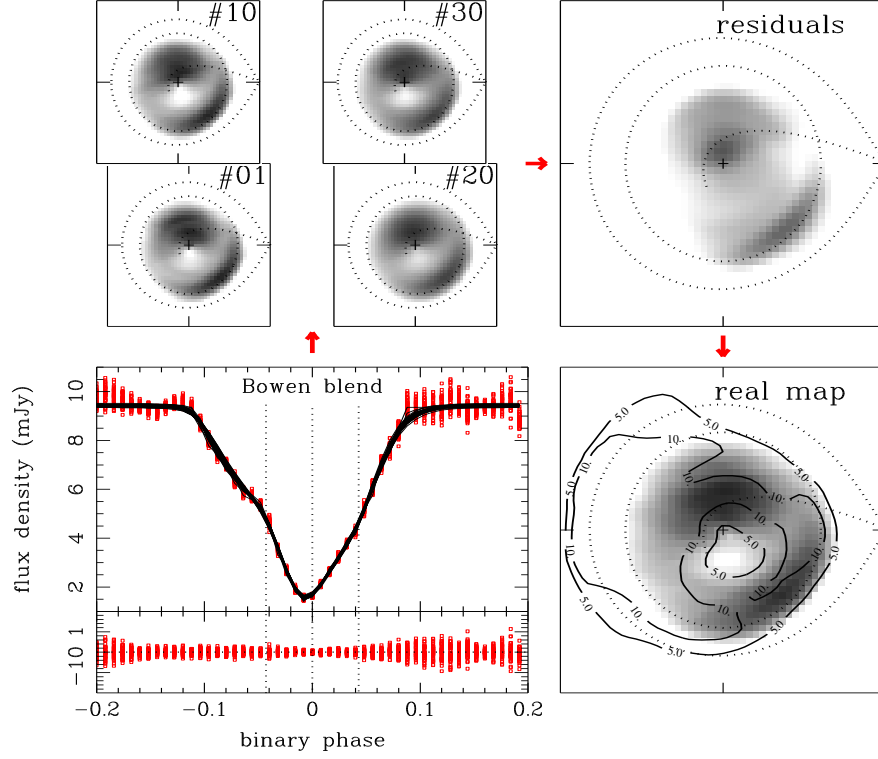


Fig. 5 Computing the statistical significance of an eclipse map from the uncertainties in the data light curve. Lower left panels: A set of 50 randomised light curves (dots) and corresponding eclipse mapping models (solid lines) superimposed in phase. The bottom panel shows these light curves after subtraction of the real data light curve. The scatter depicts the uncertainty in the flux at each phase. Top left panels: a sample of 4 of the eclipse maps from the randomised light curves, in a logarithmic grayscale. The notation is similar to that of Fig. 4. Top right panel: the map of the standard deviations with respect to the mean intensity (the “residuals” map). Lower right panel: the eclipse map from the real data light curve. Contour lines for $S/N = 5$ and 10 are overplotted; features in the eclipse maps are statistically significant at or above the 5σ confidence level.

5.1 Spectral Mapping: Spatially-resolved Disc Spectra

The eclipse mapping method is capable of delivering spatially-resolved spectra of accretion discs when the technique is applied to time-resolved eclipse spectrophotometric data, providing the best example of its ability to disentangle the light from different emission sources in the binary. The time-series of spectra is divided up into numerous (~ 100) spectral bins and light curves are extracted for each bin. The light curves are then analysed to produce a series of monochromatic eclipse maps

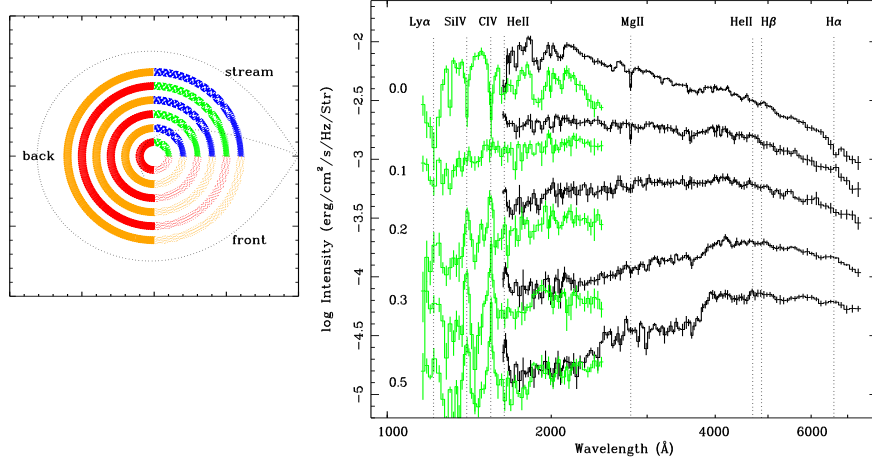


Fig. 6 An example of spectral mapping, from HST/FOS UV-optical eclipse spectroscopy of the nova-like variable UX UMa. Left panel: a schematic diagram of the eclipse map, with the annular regions used to extract spatially resolved spectra. The disc is divided into three major azimuthal regions (the back side, the front side, and the quarter section containing the gas stream trajectory), and into a set of 6 concentric annuli with radius increasing in steps of $0.1 R_{L1}$ and of width $0.05 R_{L1}$. Right panel: Spatially resolved spectra of the back region of the UX UMa accretion disc in two occasions (August 1994 in green; November 1994 in black). The spectra were computed for the set of concentric annular sections shown in the left panel. The most prominent line transitions are indicated by vertical dotted lines. From [10].

covering the whole spectrum. Finally, the maps are combined to obtain the spectrum for any region of interest on the disc surface [47].

The spectral mapping analysis of nova-like variables [47, 49, 10, 13, 29] shows that their inner accretion disc is characterised by a blue continuum filled with absorption bands and lines which cross over to emission with increasing disc radius (Fig. 6). The continuum emission becomes progressively fainter and redder as one moves outwards, reflecting the radial temperature gradient. These high mass-accretion ($\sim 10^{-8} - 10^{-9} M_{\odot} \text{ yr}^{-1}$) discs seem hot and optically thick in their inner regions and cool and optically thin in their outer parts. The spectrum of the infalling gas stream in UX UMa [10] and UU Aqr [13] is noticeably different from the disc spectrum at the same radius, suggesting the existence of gas stream “disc-skimming” overflow that can be seen down to $R \simeq (0.1 - 0.2) R_{L1}$.

In contrast, spatially-resolved spectra of low-mass accretion ($\sim 10^{-9} - 10^{-11} M_{\odot} \text{ yr}^{-1}$), quiescent dwarf nova show that the lines are in emission at all disc radii [53]. The observed differences between the spectra of the disc hemisphere farther from and closer to the L1 point might be interpreted in terms of chromospheric emission from a disc with non-negligible opening angle (i.e., a limb-brightening effect).

The spectrum of the uneclipsed component both for the nova-like systems and quiescent dwarf novae shows strong emission lines and the Balmer jump in emission indicating that the uneclipsed light has an important contribution from optically thin

gas (e.g., [13]). The lines and optically thin continuum emission are most probably emitted in a vertically extended disc chromosphere + wind [9, 38]. This additional source of radiation may be responsible both for flattening the ultraviolet spectral slope and for filling in the Balmer jump of the optically thick disc spectrum, and might explain the historical difficulties in fitting integrated disc spectrum with stellar atmosphere disc models [61, 25, 41, 39].

The uneclipsed spectrum of UX UMa at long wavelengths is dominated by a late-type spectrum that matches the expected contribution from the mass-donor star [49]. Thus, the uneclipsed component provides an interesting way of assessing the spectrum of the mass-donor star in eclipsing CVs. This is a line of research yet to be properly explored, which could largely benefit from near- and mid-infrared spectroscopy of eclipses.

Spectral mapping is also useful to isolate the spectrum of the WD, represented by the central pixel of the eclipse map. A stellar atmosphere model fit to the extracted white dwarf spectrum for the dwarf nova V2051 Oph yields the WD temperature and an independent estimate of the distance to the binary [53].

5.2 Time-lapse Mapping: Dwarf Nova Outbursts

Eclipse maps give snapshots of the accretion disc at a given time. Time-resolved eclipse mapping may be used to track changes in the disc structure, e.g., to assess variations in mass accretion rate or to follow the evolution of the surface brightness distribution through a dwarf nova (DN) outburst cycle.

DN outbursts are explained in terms of either (i) the time dependent response of a viscous accretion disc to a burst of mass transfer from the donor star (the mass transfer instability model, MTIM, e.g., [17]), or (ii) a limit-cycle behaviour driven by a thermal-viscous disc-instability (the disc-instability model, DIM, e.g., [40, 24]), in which matter progressively accumulates in a low viscosity disc (quiescence) until a critical surface density is reached at a given radius, causing a heating wave to switch the disc to a high viscosity regime (outburst) that allows the gas to diffuse rapidly inwards and onto the white dwarf. There is a set of distinct predictions from these models that might be critically tested with time-lapse eclipse mapping [3].

An example of time-lapse eclipse mapping is given in Fig. 7. Eclipse maps covering the full outburst cycle of the dwarf nova EX Dra [7] show the formation of a one-armed spiral structure at the early stages of the outburst and reveal how the disc expands during the rise until it fills most of the primary Roche lobe at maximum light. During the decline stage, the disc becomes progressively fainter until only a small bright region around the WD is left at minimum light. The evolution of the radial temperature distribution shows the presence of an outward-moving heating wave during rise and of an inward-moving cooling wave in the decline.

The temperatures of the EX Dra outbursting disc are above those expected for the hot, ionised outbursting disc gas in the DIM framework [60, 40], and the cooling wave decelerates as it travels inwards [7]. Since these results are consistent with both

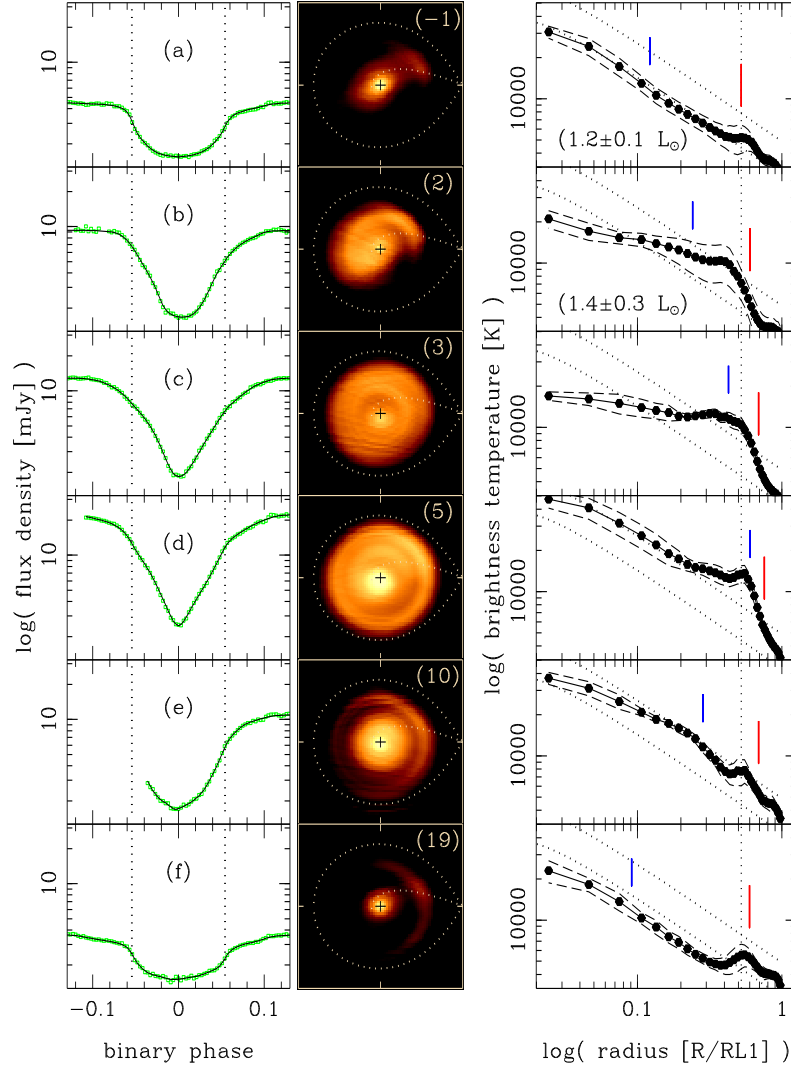


Fig. 7 Time-lapse eclipse mapping of the dwarf nova EX Dra along its outburst cycle. Left-hand panels: Data (dots) and model (solid line) light curves in (a) quiescent, (b) early rise, (c) late rise, (d) outburst maximum, (e) early decline, and (f) late decline stages. Vertical dotted lines mark ingress/egress phases of disc centre. Middle panels: eclipse maps in a false colour blackbody logarithmic grayscale. The notation is similar to that of Fig. 2. The numbers in parenthesis indicate the time (in days) elapsed since outburst onset. Right-hand panels: azimuthal-averaged radial brightness temperature distributions for the eclipse maps in the middle panels. Dashed lines show the $1\text{-}\sigma$ limit on the average temperature for a given radius. A dotted vertical line depicts the radial position of the bright spot in quiescence; vertical ticks mark the position of the outer edge of the disc (red) and the radial position at which the disc temperature falls below 11000 K (blue). Steady-state disc models for mass accretion rates of $\log \dot{M} = -8.0$ and $-9.0 M_{\odot} \text{ yr}^{-1}$ are plotted as dotted lines for comparison. Numbers in parenthesis list the integrated disc luminosity. From [7].

DIM and MTIM, they offer no power to discriminate between these models. However, the same eclipse mapping study reveals that the radial temperature distribution in quiescence follows the $T \propto R^{-3/4}$ law of opaque steady-state discs (Fig. 7(a)), and that this quiescent state is reached only 2 d after the end of the outburst. Both results indicate that the viscosity of its quiescent disc is as large as in outburst – in contradiction with DIM and in agreement with predictions of the MTIM. In addition, the early rise map shows evidence of enhanced gas stream emission, indicative of an enhanced mass transfer rate at this early outburst stage (Fig. 7(b)). The integrated disc luminosity at early rise ($1.4 \pm 0.3 L_{\odot}$) is comparable to that in quiescence ($1.2 \pm 0.1 L_{\odot}$), and is not enough to support the idea that the enhanced mass transfer could be triggered by an increased irradiation of the mass donor by the accretion disc. This led to the conclusion that the observed enhanced mass transfer at early rise is not a consequence of the ongoing outburst, but its cause – suggesting that the outbursts of EX Dra are powered by bursts of mass transfer [3].

Time-lapse eclipse mapping studies were also performed for the dwarf novae Z Cha [63], OY Car [51, 23], IP Peg [19], V2051 Oph [12], and HT Cas [36, 26].

5.3 Flickering Mapping: Revealing the Disc Viscosity

Flickering is the intrinsic brightness fluctuation seen in light curves of T Tau stars [31], mass-exchanging binaries [1, 22] and active galactic nuclei [27]. Optical studies suggest there are two different sources of flickering in CVs: (i) the stream-disc impact region (possibly because of unsteady mass inflow or post-shock turbulence [62, 55]) and/or (ii) turbulent inner disc regions (possibly because of magneto-hydrodynamic (MHD) turbulence, unsteady WD accretion or events of magnetic reconnection at the disc atmosphere [28, 21, 37]). With its ability to spatially-resolve and to disentangle different sources, flickering mapping has been a useful tool to confirm and extend this scenario. As an added bonus, if the disc-related flickering is caused by MHD turbulence, one may infer the radial run of the disc viscosity parameter α_{ss} [54] from the relative flickering amplitude, (σ_D/D) [28],

$$\alpha_{ss}(R) \simeq 0.23 \left[\frac{R}{50H} \right] \left[\frac{\sigma_D(R)}{0.05D(R)} \right]^2, \quad (11)$$

where H is the disc scale height.

From a large, uniform ensemble of light curves of a given CV it is possible to separate the steady-light component (the average flux in a given phase bin), low- and high-frequency flickering amplitudes (the scatter with respect to the average flux, computed with the ensemble [18] and single [21] methods) as a function of binary phase, to derive corresponding maps of surface brightness distributions from their eclipse shapes and, thereafter, to compute the radial run of the relative amplitude of the disc flickering component [5, 6].

Flickering mapping of the DN V2051 Oph reveals that the low-frequency flickering arises mainly in an overflowing gas stream and is associated with the mass transfer process. The high-frequency flickering originates in the accretion disc and has a relative amplitude of a few percent, independent of disc radius and brightness level, leading to large values $\alpha_{ss} \simeq (0.1 - 0.2)$ at all disc radii [5].

Figure 8 shows the results of the eclipse mapping analysis of an extensive data set of optical light curves of the dwarf nova HT Cas [3]. These observations frame a 2 d transition from a low state (largely reduced mass transfer rate) back to quiescence, allowing the application of both time-lapse and flickering mapping techniques to derive independent estimates of α_{ss} . In the low state, the gas stream hits the disc at the circularisation radius R_{circ} [60], and the accretion disc has its smallest possible size. The disc fast viscous response to the onset of mass transfer, increasing its brightness and expanding its outer radius at a speed $v \simeq +0.4 \text{ km s}^{-1}$, implies $\alpha_{ss} \simeq 0.3 - 0.5$. The newly added disc gas reaches the WD at disc centre soon after mass transfer recovery (~ 1 d), also implying a large disc viscosity parameter, $\alpha_{ss} \simeq 0.5$. Flickering mapping reveal a minor, low-frequency BS-stream flickering component in the outer disc, plus a main disc flickering component the amplitude of which rises sharply towards disc centre (Fig. 8), leading to a radial dependency $\alpha_{ss}(R) \propto R^{-2}$ with $\alpha_{ss} > 0.1$ for $R < R_{\text{circ}}$ – in agreement with the time-lapse results.

A similar analysis was performed for the DN V4140 Sgr [4]. Eclipse mapping in quiescence indicate that the steady-light is dominated by emission from an extended disc with negligible contribution from the WD, suggesting that efficient accretion through a high-viscosity disc is taking place. Flickering maps show an asymmetric source at disc rim (BS-stream flickering) and an extended central source (disc flickering) several times larger in radius than the WD. Unless the thin disc approximation breaks down, the relative amplitude of the disc flickering leads to large α_{ss} 's in the inner disc regions ($\simeq 0.2 - 1.0$), which decrease with increasing radius.

In contrast, in the nova-like UU Aqr optical flickering arises mainly in tidally-induced spiral shocks in its outer disc [6]. Assuming that the turbulent disc model applies, its disc viscosity parameter increases outwards and reaches $\alpha_{ss} \sim 0.5$ at the position of the shocks, suggesting that they might be an effective source of angular momentum removal of disc gas.

5.4 3D Eclipse Mapping: Disc Opening angle & Superhumps

Standard eclipse mapping assumes a simple flat, geometrically thin disc model. Real discs may however violate this assumption in the limit of high \dot{M} . Disc half-opening angles of $\beta \geq 4^\circ$ are predicted for $\dot{M} \geq 5 \times 10^{-9} M_\odot \text{ yr}^{-1}$ [43]. At large inclinations ($i \geq 80^\circ$) this may lead to artificial front-back asymmetries in the eclipse map because of the different effective areas of surface elements in the near and far sides of a flared disc as seen by an observer on Earth. Furthermore, the assumption that the emitted radiation is independent of orbital phase implies that any out-of-eclipse

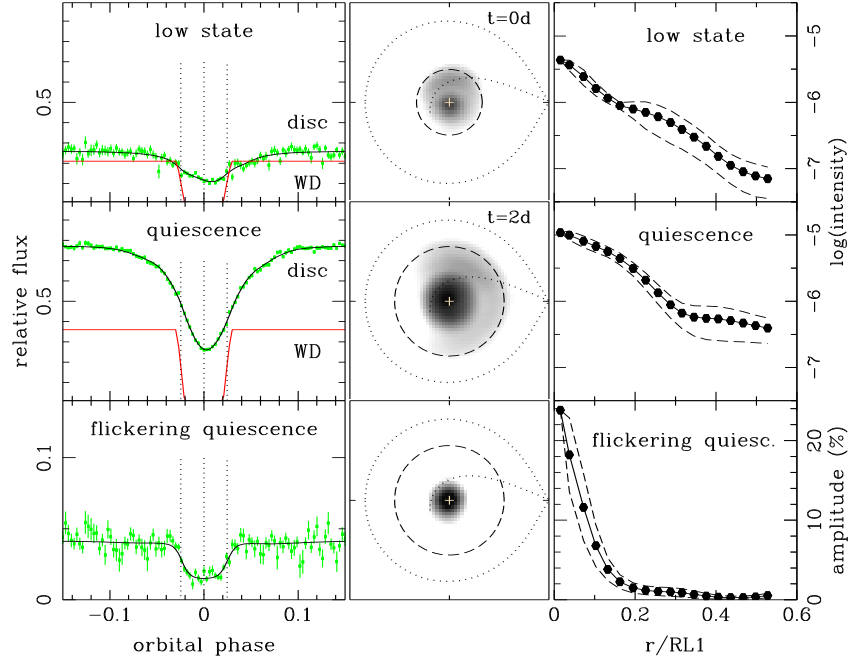


Fig. 8 Left-hand panels: data (green dots) and eclipse mapping model (black lines) disc light curves, and the extracted light curve of the WD (red lines). Top and middle panels show, respectively, the low state and quiescence steady-light component, while the lower panel shows the high-frequency ($f > 3.3\text{mHz}$) flickering curve. Middle panels: the corresponding eclipse maps in a logarithmic grayscale. The notations is similar to that of Fig. 1. Dashed circles mark the outer disc radius in each case. Right-hand panels: azimuthal-averaged radial intensity (top, middle) and flickering amplitude in percent (bottom) distributions for the eclipse maps in the middle panels. Dashed lines show the 1- σ limit on the average value for a given radius.

brightness change (e.g., orbital modulation due to BS anisotropic emission) has to be removed before the light curve can be analysed³.

A step to overcome these limitations is to go beyond the standard assumptions allowing the eclipse mapping surface to become three-dimensional. This leads to 3D eclipse mapping [50]. For example, with the inclusion of a disc rim in the eclipse mapping method, the out-of-eclipse modulation can be modelled as the foreshortening of an azimuthal-dependent brightness distribution in the disc rim [19]. This procedure allows one to recover the azimuthal (phase) dependency of the BS emission. Moreover, motivated by the front-back asymmetry that appeared in the flat-disc map and by the difficulties in removing the asymmetry with the assumption of an uneclipsed component, [45] introduced a flared disc in their eclipse mapping

³ This is usually done by fitting a spline function to the phases outside eclipse, dividing the light curve by the fitted spline, and scaling the result to the spline function value at phase zero (e.g., [9]).

of ultraviolet light curves of Z Cha at outburst. They found that the asymmetry vanishes and the disc is mostly axi-symmetric for a disc half-opening angle of $\beta = 6^\circ$.

In 3D eclipse mapping, the mapping surface usually consists of a grid of N_1 pixels on a conical surface centred at the WD position and inclined at a half-opening angle β with respect to the orbital plane, plus a circular rim of N_2 pixels orthogonal to the orbital plane at a distance R_d ($< R_{L1}$) from disc centre. An *entropy landscape* technique [48] may be used to cope with the extra degree of freedom that comes along with the additional geometry parameters β and R_d . Simulations [4] show that if an eclipse mapping reconstruction is performed with the wrong choice of β and R_d , the code develops artefacts in the brightness distribution in order to compensate for the incorrect parameters. Eclipse maps with these spurious, additional structures have lower entropy than the map with the correct choice of β and R_d . Therefore, the best-fit geometry can be found by searching the space of parameters for the pair of (β, R_d) values of highest entropy (Fig. 9, left-hand panels).

An example of 3D eclipse mapping is shown in Fig. 9, where the technique was applied to study the evolution of the accretion disc surface brightness of the DN V4140 Sgr in a superoutburst [4]. The entropy landscape analysis indicates that the accretion disc is geometrically thin both in outburst ($\beta = 1.0^\circ \pm 0.5^\circ$) and in quiescence ($\beta = 0.5^\circ \pm 0.5^\circ$); it fills the primary Roche lobe in outburst and progressively shrinks to about half this size in quiescence. They also find that the disc is elliptical in outburst and decline, with an eccentricity $e = 0.13$. At both outburst stages, the disc orientation is such that superhump maximum occurs when the mass-donor star is aligned with the bulge of the elliptical disc. This lends observational support for the tidal resonance instability model of superhumps [64, 32, 42].

Additional observational support for the presence of elliptical precessing discs in CVs come from the eclipse mapping analyses of light curves of the DN Z Cha in superoutburst [44] and of the permanent superhumper V348 Pup [46].

6 Summary

Eclipse mapping is a unique, powerful technique to investigate:

- Accretion disc spectra (allowing one to separate the disc atmosphere emission at different distances from disc centre, and to isolate the spectrum of the WD, BS, a possibly outflowing disc wind, and even the faint, red mass-donor star);
- Accretion disc structures (such as gas stream overflow, tidally-induced spiral shocks, elliptical precessing discs, and magnetic accretion curtains);
- Time evolution of accretion discs (tracing the mass and angular momentum redistribution throughout dwarf nova outbursts, or to follow brightness changes caused by lighthouse effects in discs with fast spinning, magnetic WDs);
- Accretion disc viscosity (either via flickering mapping or by measuring the velocity of transition waves during dwarf nova outbursts with time-lapse mapping).

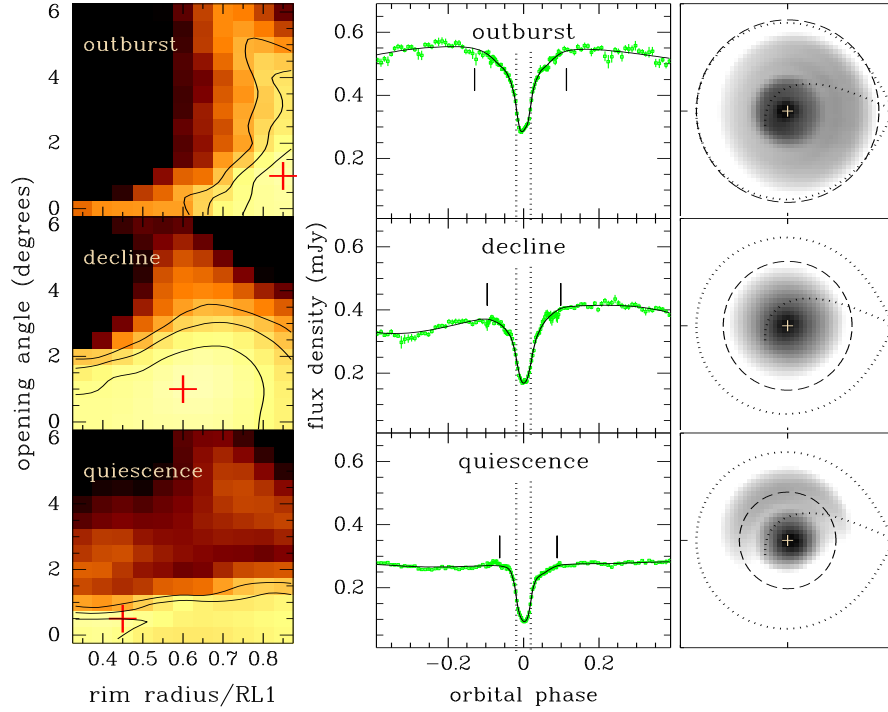


Fig. 9 3D eclipse mapping of V4140 Sgr. Left panels: entropy landscape for the outburst (top), decline (middle) and quiescence (bottom) light curves in a blackbody false-colour scale. Regions in yellow have higher entropy. A red cross marks the combination of disc half-opening angle β and rim radius R_d of highest entropy. Middle panels: data (dots) and model (solid line) light curves for the pair of (β, R_d) values of highest entropy in each case. Vertical dotted lines mark the ingress/egress phases of the WD, while vertical tick marks depict the phases of eclipse ingress/egress. Right panels: corresponding eclipse maps in a logarithmic grayscale. The notation is similar to that of Fig. 2. Dashed circles show the best-fit disc rim radius. From [4].

Acknowledgements RB acknowledges financial support from CNPq/Brazil through grant no. 308 946/2011-1.

References

1. Augusteijn, T., Karatasos, K., Papadakis, M., et al. 1992, A&A 265, 177
2. Baptista, R., 2001, In: *Astromotography: Indirect Imaging Methods in Observational Astronomy, Lecture Notes in Physics 573*, eds. H. M. J. Boffin, D. Steeghs & J. Cuypers (Berlin: Springer), 307
3. Baptista, R., 2012, Mem. S. A. It. 83, 530
4. Baptista, R., Borges, B., Oliveira, A. S., 2015, AJ, in press
5. Baptista, R., Bortoletto, A., 2004, AJ 128, 411

6. Baptista, R., Bortoletto, A., 2008, ApJ 676, 1240
7. Baptista, R., Catalán, M. S., 2001, MNRAS 324, 599
8. Baptista, R., Harlaftis, E. T., Steeghs, D., 2000, MNRAS 314, 727
9. Baptista, R., Horne, K., Hilditch, R. W., et al., 1995, ApJ 448, 395
10. Baptista, R., Horne, K., Wade, R. A., et al., 1998, MNRAS 298, 1079
11. Baptista, R., Morales-Rueda, L., Harlaftis, E. T., et al., 2005, A&A 444, 201
12. Baptista, R., Santos, R. F., Faúndez-Abans, M., Bortoletto, A., 2007, AJ 134, 867
13. Baptista, R., Silveira, C., Steiner, J. E., Horne, K., 2000, MNRAS 314, 713
14. Baptista, R., Steiner, J. E., 1991, A&A 249, 284
15. Baptista, R., Steiner, J. E., 1993, A&A 277, 331
16. Baptista, R., Steiner, J. E., Horne, K., 1996, MNRAS 282, 99
17. Bath, G. T., 1975, MNRAS 171, 311
18. Bennie, P. J., Hilditch, R., Horne, K., 1996, in *Cataclysmic Variables and related objects*, IAU Coll. 158, eds. A. Evans & J. Wood (Dordrecht: Kluwer), 33
19. Bobinger, A., Horne, K., Mantel, K. H., Wolf, S., 1997, A&A 327, 1023
20. Bobinger, A., 2000, A&A 357, 1170
21. Bruch, A., 1992, A&A 266, 217
22. Bruch, A., 2000, A&A 359, 998
23. Bruch, A., Beele, D., Baptista, R., 1996, A&A 306, 151
24. Cannizzo, J. K., 1993, ApJ 419, 318
25. La Dous, C., 1989, A&A 211, 131
26. Feline, W. J., Dhillon, V. S., Marsh, T. R., et al., 2005, MNRAS 364, 1158
27. Garcia, A., Sodr , L., Jablonski, F. J., Terlevich, R. J., 1999, MNRAS 309, 803
28. Geertsema, G. T., Achterberg, A., 1992, A&A 255, 427
29. Groot, P. J., 1999, *Optical Variability in Compact Source*, PhD Thesis, Univ. of Amsterdam
30. Harlaftis, E. T., Baptista, B., Morales-Rueda, L., et al., 2004, A&A 417, 1063
31. Herbst, W., Shevchenko, K. S., 1999, AJ 118, 1043
32. Hirose, M., Osaki, Y., 1990, PASJ 42, 135
33. Horne, K., 1985, MNRAS 213, 129
34. Horne, K., Marsh, T. R., 1986, In: *The Physics of Accretion onto Compact Objects*, eds. K. Mason, P. Charles (Springer-Verlag, Berlin), 1
35. Horne, K., 1993, In: *Accretion Disks in Compact Stellar Systems*, ed. J. C. Wheeler (World Scientific Publ. Co., Singapore), 117
36. Ioannou, Z., Naylor, T., Welsh, W. F., et al., 1999, MNRAS 310, 398
37. Kawaguchi, T., Mineshige, S., Machida, M., et al., 2000, PASJ 52, L1
38. Knigge, C., Drew, J. E., 1997, ApJ 486, 445
39. Knigge, C., Long, K. S., Wade, R. A., et al., 1998, ApJ 499, 414
40. Lasota, J. P., 2001, New Astronomy Reviews 45, 449
41. Long, K. S., Wade, R. A., Blair, W. P., Davidsen, A. F., Hubeny, I., 1994, ApJ 426, 704
42. Lubow, S. H., 1994, ApJ 432, 224
43. Meyer, F., Meyer-Hofmeister, E., 1982, A&A 106, 34
44. O'Donoghue, D., 1990, MNRAS 246, 29
45. Robinson, E. L., Wood, J. E., Wade, R. A., 1999, ApJ 514, 952
46. Rolfe, D., Haswell, C. A., Patterson, J., 2000, MNRAS, 317, 759
47. Rutten, R. G. M., Dhillon, V. S., Horne, K., et al., 1993, Nature 362, 518
48. Rutten, R. G. M., Dhillon, V. K., 1994, A&A 288, 773
49. Rutten, R. G. M., Dhillon, V. S., Horne, K., Kuulkers, E., 1994, A&A 283, 441
50. Rutten, R. G. M., 1998, A&AS 127, 581
51. Rutten, R. G. M., Kuulkers, E., Vogt, N., van Paradijs, J., 1992, A&A 254, 159
52. Rutten, R. G. M., van Paradijs, J., Tinbergen, J., 1992, A&A 260, 213
53. Saito, R. K., Baptista, R., 2006, AJ 131, 2185
54. Shakura, N. I., Sunyaev, R. A., 1973, A&A 24, 337
55. Shu, F. H., 1976, in *Structure and Evolution of Close Binary Systems*, P. Eggleton, S. Mitton & J. Whelan (eds.), Dordrecht, 253
56. Skilling, J., Bryan, R. K., 1984, MNRAS 211, 111

- 57. Skilling, J., 1987, In: *Maximum Entropy and Bayesian Methods in Applied Statistics*, ed. J. H. Justice (Cambridge University Press, Cambridge), 156
- 58. Spruit, H. C., 1994, A&A 289, 441
- 59. Steeghs, D., Harlaftis, E. T., Horne, K., 1997, MNRAS 290, L28
- 60. Warner, B., 1995, *Cataclysmic Variable Stars* (Cambridge University Press, Cambridge)
- 61. Wade, R. A., 1988, ApJ 335, 394
- 62. Warner, B., Nather, R. E., 1971, MNRAS 152, 219
- 63. Warner, B., O'Donoghue, D., 1988, MNRAS 233, 705
- 64. Whitehurst, R., 1988, MNRAS 232, 35
- 65. Wood, J. H., 1994, In: *Interacting Binary Stars*, ASP Conference Series, Vol. 56, ed. A. W. Shafter (ASP, USA), 48